Progress in Additive Manufacturing (2025) 10:10533–10547
https://doi.org/10.1007/s40964-025-01313-z

RESEARCH

Detection of sub-superficial defects by infrared thermography in parts made by powder bed fusion with electron beam

Silvio Defanti[1] · Simone De Giorgi[2] · Giovanni Rizza[2] · Giulia Colombini[1] · Lucia Denti[1] · Manuela Galati[2]

Received: 28 April 2025 / Accepted: 16 August 2025 / Published online: 25 August 2025

Abstract
The study explores Joule heating infrared thermography as a cost-effective alternative to computed tomography (CT) for detecting subsurface defects in parts produced by powder bed fusion with electron beam (PBF-EB). The primary objective was to quantify how surface roughness typical of different build orientations in PBF-EB affects thermographic data reliability. Simplified intentional defects of various sizes and depths were created in Ti6Al4V custom-samples under various target surfaces, whose morphology was characterized by confocal microscopy. CT scans provided accurate defect dimensions and revealed that sintered powder within defects does not significantly affect thermographic detection and can be treated as voids, paving the way to the application of the method to closed defects. The research led to the development and calibration of a reliable automated thermographic inspection protocol, the definition of best practices and key performance indicators for detectability, and the initiation of defect detectability maps tailored to the distinctive anisotropic features of additively manufactured parts.

Keywords Electron beam powder bed fusion · Thermography · Inspection · Defects

1 Introduction

Active thermography has emerged as a powerful non-destructive testing (NDT) technique for assessing the structural integrity of components [1, 2]. By monitoring thermal responses to external stimuli, in the ex-situ version it enables the rapid and non-invasive detection of subsurface defects [3], such as pores, cracks, or lack of fusion. Based on the principle of thermal wave propagation [4], thermographic inspection usually involves stimulating the surface of a component with an external heat source [5, 6] and recording the resulting thermal response using an infrared (IR) camera [3]. Subsurface discontinuities alter the heat flow, leading to measurable anomalies in the thermal profile.

However, the effectiveness of thermography is strongly influenced by various factors [7]. The detectability of defects in thermography depends on both their size and their proximity to the surface, with larger defects and those closer to the surface being more easily detected due to the more pronounced thermal anomalies they produce on the inspected surface [7]. Promising results have been reported for IRT with Joule excitation, which has proven to be a low-cost and time-efficient method for offline inspection of surface-emergent cracks [8]. Empirical guidelines suggest that defects with a size-to-depth ratio greater than 2 generally ensure reliable detectability. This threshold is difficult to overcome even with recent advances such as the use of pixelated patterns generated by laser-coupled high-power DLP projector technology to achieve photothermal super resolution reconstruction [9]. While this approach is highly innovative, it still requires further development before it can be applied

✉ Silvio Defanti
silvio.defanti@unimore.it

Simone De Giorgi
simone.degiorgi@polito.it

Giovanni Rizza
giovanni.rizza@polito.it

Giulia Colombini
giulia.colombini@unimore.it

Lucia Denti
lucia.denti@unimore.it

Manuela Galati
manuela.galati@polito.it

[1] Department of Engineering “Enzo Ferrari”, University of Modena and Reggio Emilia, Modena, Italy

[2] Department of Management and Production Engineering, Politecnico di Torino, Torino, Italy

in industrial settings. Other recent studies have lowered the size-to-depth limit to 1 or even 0.5 [10, 11]. In addition, the characteristics of the surface of the component are of particular importance; in particular, surface roughness plays a decisive role, as it significantly influences the emissivity [12, 13]. Rough reflective surfaces tend to exhibit a variable and higher emissivity compared to smooth or coated ones [14], which can lead to inconsistent temperature readings. Furthermore, surface irregularities can emit, scatter, and absorb thermal radiation unevenly [15], distorting the thermal gradients that are essential for defect detection. To mitigate these effects, coatings with high emissivity are often applied prior to inspection [7]. However, this operation is associated with additional time and costs and is particularly problematic for intricate geometries or components that cannot be coated uniformly.

Compared to other manufacturing processes for metallic components, the challenges of thermography for ex-situ defect detection are especially relevant in the context of additive manufacturing (AM) [16], where defects due to process instabilities, such as lack of fusion, are small and surface roughness is inherently high and varies significantly with surface orientation relative to the build direction. AM builds up components layer by layer, resulting in a roughness profile that is highly dependent on the raw material, process parameters, and surface orientation [17, 18]. For instance, downskin surfaces typically exhibit poorer surface quality than upskin or side surfaces due to factors such as insufficient heat dissipation and lack of support during fabrication [19].

In this area, several studies have evaluated the potential of passive IRT for in situ monitoring, for example to reconstruct the thermal history of a component and predict the resulting mechanical properties and porosity formation [20]. A similar in-situ approach, combined with optical tomography, has been shown to be potentially effective for monitoring thermal effects associated with the intentional non-exposure of multiple layers, with the aim of analyzing melt pool penetration and the healing ability of subsequent layer exposure to prevent the formation of defects [21].

Among AM technologies for metals, Powder Bed Fusion with Electron Beam (PBF-EB) stands out for its ability to produce high-performance parts with efficient thermal management and reduced support structures [22]. However, it also tends to generate surfaces with pronounced roughness [19]. This roughness is largely due to the use of relatively large powder particles (between 45 µm and 150 µm), the deposition of thick layers (over 50 µm), and process strategies such as preheating [23], which contribute to an irregular surface morphology due to the partially sintered powder surrounding the component surfaces [22]. While there are numerous research papers on the effects of surface roughness at various levels, such as fatigue behaviour in AM components (e.g. [17, 24, 25]), a discussion on how PBF-EB surfaces may affect the Infrared Thermography (IRT) inspection method for ex-situ defect detection is still pending. On the other hand, the growing interest in IRT has also been highlighted by the introduction of this technique in the recent ISO/ASTMTR52905 for NDT quality control of AM components [26]. The scientific literature includes several noteworthy studies on the use of thermography for defect detection in parts produced by AM processes using laser sources—both in powder flow configurations [27] and, more extensively, in powder bed systems [28–31]. Optical excitation using lasers or flash lamps has been numerically simulated and experimentally validated for detecting defects as small as 0.35 mm in size and approximately 0.4 mm in depth [28]. More recently, the same authors applied pulsed thermography to the detection of spherical defects, focusing on optimized post-processing techniques and robust statistical protocols. As expected for surface-heating methods, detection was successful primarily for relatively large and shallow defects [29] and was compared to eddy current testing in [32]. In-situ thermographic testing using the processing laser of a PBF-LB/M setup as an excitation source is being investigated as a particularly effective approach to qualifying components during their construction [20, 33, 34].

While these studies demonstrate the potential of thermographic techniques for in situ monitoring and defect detection in laser-based AM processes, they do not address the specific challenges posed by the PBF-EB process, nor do they consider the influence of surface morphology on thermographic signal reliability. The systematic investigation of how surface roughness—resulting from different build orientations in AM—affects the quality and reliability of thermographic data, an aspect largely overlooked in prior research.

Given these considerations, PBF-EB represents the natural candidate to understand how surface roughness affects thermographic response, which is essential for improving defect detection in AM components. In this study, the relationship between surface roughness and the quality of the thermographic signal is investigated by analysing the upskin, downskin, and side surfaces of custom-designed Ti6Al4V samples containing intentionally unfused cylindrical defects of controlled size and depth. Each defect is open on one side and sealed just beneath the inspected surface. Four identical samples were built with different orientations to assess the influence of surface morphology on defect visibility. Surface topography was characterized using confocal optical microscopy, while defect geometry and position were verified via X-ray computed tomography. Thermographic testing was performed by applying electric current to the samples and recording the thermal response

using an IR camera. Infrared data were processed in MATLAB to compute the signal-to-noise ratio (SNR) as a quantitative indicator of defect detectability and to extract defect size.

The objective is to quantify the influence of roughness on the reliability of the thermographic data and to propose practical guidelines for defect detection in as-built PBF-EB components. The analysis, therefore, considers different sizes and depths of the intentionally created defect.

2 Materials and methods

2.1 Samples design

The study was conducted on specimens with a constant square cross-section of 10 mm × 10 mm and a length of 60 mm, featuring intentional defects. Focusing on cylindrical defects, the study considered various sizes and configurations to establish an inspection protocol and start developing a detectability map that should cover all the typical and more complex defects of PBF-EB in future developments. In this first step, cylindrical defects were designed with one side open and the other sealed just beneath the surface under investigation, hereafter "target surface", to which the axis of the holes was perpendicular. An open defect is not entirely representative of anomalies typically found in industrial parts built by PBF-EB, where unintended defects are instead filled with sintered powder. Open defects, which can partially empty during de-powdering, were chosen to ensure more effective thermal signal generation and clearer detectability during thermographic analysis. This approach aims to use these defects as reference features for the development and calibration of thermographic inspection, with a specific focus on the impact on the detection of the distinctive surface finish obtained by PBF-EB.

Defects of varying diameter (0.5 mm to 1 mm, hereafter called size) and depths (0.25 mm to 2 mm) were seeded under different target surface orientations in the PBF-EB system. Even if the chosen configurations are certainly at the upper limit of the size range and at the lower limit of the depth values relevant for industrial parts, this methodology allows the development of a reliable detection framework and the identification of best practices in applications that are at the boundary of detectability, with the aim of being applied to more challenging defects. Four cylindrical defects were designed and produced within each sample, oriented perpendicularly to the electrical current/heat flow and spaced to avoid interactions. Figure 1 shows the geometry and relative position of the defects, target surface, and depth. Holes were added at the ends of the sample to facilitate the attachment of electrical cables.

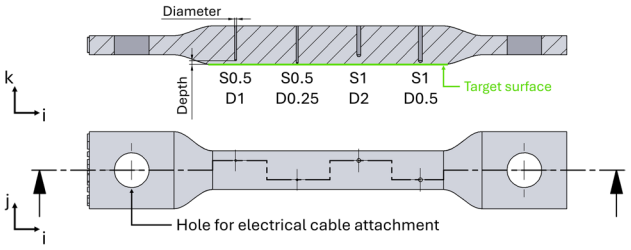

Fig. 1 Geometry of the samples showing the placement of the defects, their size, and depth below the target surface and the holes for electrical cable attachment. A local i, j, k coordinate system is defined to differentiate it from the coordinate system employed during the manufacturing of the sample. The building orientation depends on the selected target surface. The current flows along the i-direction

Four samples with identical defects were fabricated, each with distinct build orientations to investigate the influence of the manufacturing direction on both defect formation and target surface morphology. Surface types considered were: Upskin, Side, Downskin built on loose powder and Downskin built directly on the build platform and subsequently detached from it. Details of the samples and defect specifications are summarized in Table 1.

The following key variables are therefore considered, assessing their impact on defect detectability:

- Build orientation: it influences the build-up of the defect;
- Defect size and depth: both parameters strongly influence detectability, particularly the size/depth ratio.
- Surface Type: also affected by build orientation, surface type directly affects surface morphology.

2.2 Samples manufacturing

One sample of each type was produced using an Arcam A2X, an electron beam powder bed fusion system. The feedstock material consisted of commercially available Ti6Al4V ELI powder produced by ATI. According to the datasheet provided by the powder producer, this is characterised by particle sizes of 50 to 150 µm with a D10 of 54 µm, a D50 (median particle size) of 100 µm, and a D90 of 146 µm. The apparent density of the powder is 2.59 g/cm^3. Prior to melting, the build layers were preheated to a temperature of 700 °C. A layer height of 0.050 mm was employed for the production. The manufacturer's standard processing parameters for the Ti6Al4V alloy were adopted [27] including the use of Multibeam™ strategy for contour melting. After production, the samples detached themselves from the start plate without intervention and were cleaned using the blasting system in which the same

Table 1 Detailed list of the analysed samples

Sample type	Defect axis building orientation	Target surface type	Defect ID	Size [mm]	Depth [mm]	Size/depth
H-Up	Z	Upskin	S0.5_D1	0.5	1.0	0.5
			S0.5_D0.25	0.5	0.25	2.0
			S1_D2	1.0	2.0	0.5
			S1_D0.5	1.0	0.5	2.0
H-Side	Y	Side	Same as H-up			
H-Down	Z	Downskin	Same as H-up			
H-Down_plat	Z	Downskin facing platform	Same as H-up			

feedstock material was adopted. No additional operation was performed and therefore all the surfaces of the samples can be classified as "as-built".

2.3 Surface characterisation

A Nikon LV 150 optical microscope, equipped with a Confovis system, was used to analyze the surface topology of the samples. The Confovis system uses a focused laser beam to scan a sample point-by-point. It employs a pinhole aperture to eliminate out-of-focus light, which improves optical resolution and contrast. By capturing images at different optical sections, it enables the reconstruction of three-dimensional structures within the sample.

A 4.5×2.5 mm^2 area was scanned on the upskin, side, downskin, and downskin on platform surfaces. The analysis was performed using a $100\times$ objective with a layer discretization of 0.50 µm.

2.4 Tomography

The characterisation of the defects in terms of size and location — in relation to the nominal geometry — was carried out using computer tomography (CT) with a GE Phoenix V|tome|x S 240 system, operating at a voxel resolution of 20 µm. The tomographies were collected using a voltage of 160 kV and a current of 140 µA. The reconstruction and the analysis were performed using VG Studio MAX3.4. The measurement of the defects from the CT data was carried out using the tool to evaluate the distances. The measurement was repeated five times at different positions in the defect. The effective value of the distance is obtained as the average of these measures and reported as the mean value and standard deviation.

2.5 Thermography tests setup and procedure

The experimental configuration for the thermographic testing (Fig. 2a) corresponds to a typical setup for active thermography using Joule heating, where the sample is

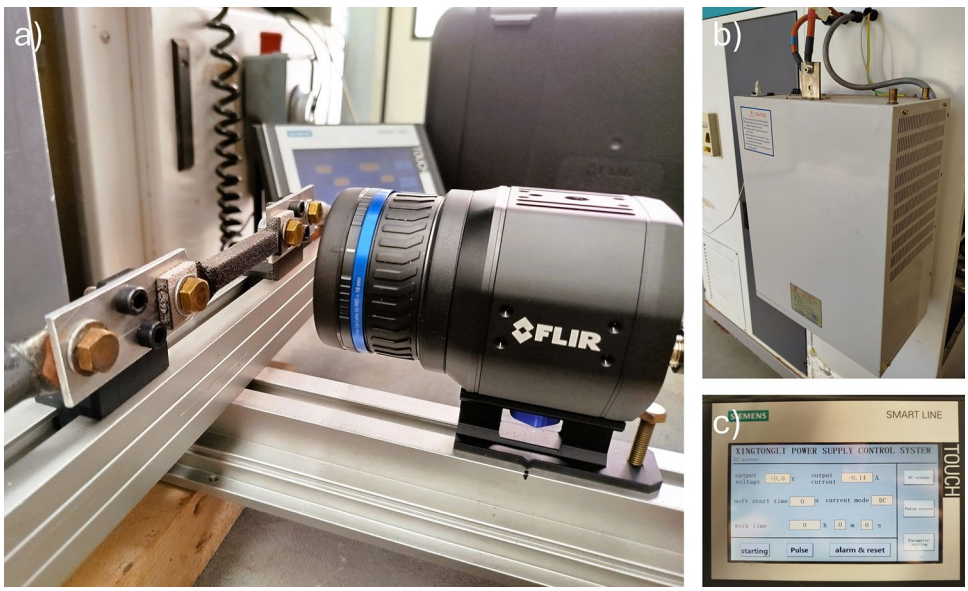

Fig. 2 Thermography test setup: **a** camera and sample positioning, **b** power supply unit, **c** power supply human–machine interface

internally heated by means of electrical current. Subsurface defects such as cracks, voids, or lack of fusion alter the local thermal conductivity and electrical resistivity, leading to measurable thermal contrasts on the surface [2]. These anomalies are captured in real time using an infrared camera. The included setup used in this study includes: a Xingtongli GKDM24-1000CVC power supply unit (Fig. 2b, c) delivering direct current up to 24 V and 1000 A, and a Teledyne FLIR A700 uncooled microbolometer infrared camera with a spectral range of 7.5 – 14 µm. The camera was mounted 40 mm from the sample, with its optical axis perpendicular to the target surface. Equipped with a 2 × FLIR macro lens (focal length: 17.5 mm, f-number: 1.1), it captured a field of view of 25.5×19.1 mm^2. With a detector array of 640×480 pixels, the system achieved a spatial resolution of 40 µm per pixel and recorded thermal frames at 30 Hz.

Initial trials indicated the need to coat the sample surfaces with matt black paint (emissivity 0.94) to suppress reflections and improve thermal signal quality. Tests were performed in a semi-enclosed chamber to limit the influence of ambient thermal radiation. After aligning and focusing the IR camera on the surface of the specimen, thermal data acquisition began and an electric current was applied for a few seconds. Prior to each trial, the apparent temperature of the sample, as measured by the infrared camera, was verified to differ by no more than 0.5 °C from the surrounding environment, in order to ensure thermal equilibrium. Each sample underwent six randomised test cycles. A preliminary test on sample H-down-plat varied the current from 20 to 800 A, measuring the resulting diameter and thermographic signal. Based on preliminary results, all defects were analysed with a potential of 1 V across the sample, resulting in approximately 200 A. In the preliminary tests, the excitation time was set at 1 min.

2.6 IR data processing

Post-processing of the infrared recordings was performed in MATLAB using the 'FLIR Science File SDK for MATLAB' to extract individual thermal frames in matrix format for detailed quantitative analysis. The first phase focused on identifying the frame with the highest thermal contrast between the defective area and the surrounding material, assessing defect visibility. To accomplish this, the signal-to-noise ratio (SNR) was computed for each frame, following the methodology described in [35, 36], as defined in Eq. (1):

$$\mathrm{SNR} = \frac{\left|\overline{T_d} - \overline{T_{nd}}\right|}{\sigma_{nd}} \tag{1}$$

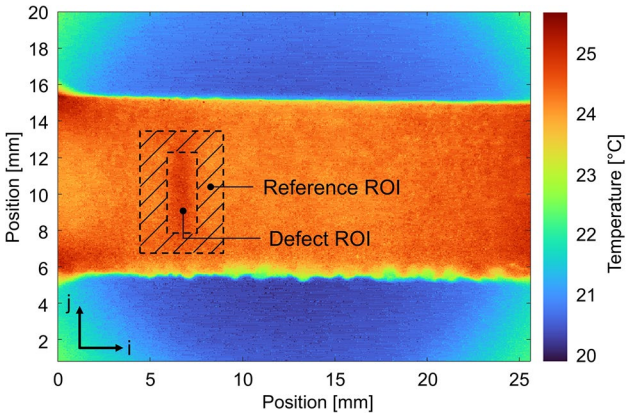

Fig. 3 Regions of interest considered for the calculation of the SNR

where:

– $\overline{T_d}$ represents the mean level of the signal in the defect region of interest (ROI), defined as a rectangular area tightly enclosing the defect (Fig. 3);

– $\overline{T_{nd}}$ denotes the mean level of the noise in the surrounding reference region, a hollow rectangular ROI obtained by offsetting the defect ROI (hatched in Fig. 3);

– σ_{nd} is the standard deviation of the noise within the reference ROI, representing the background noise level.Within this framework, the SNR is assumed to be a Key Performance Indicator (KPI) for defect detectability. A defect is considered detectable if SNR > 1, meaning that the signal is attributable to the defect background noise. The calculated SNRs are averaged over 6 measurements.

These measurements are strongly influenced by the definition of the reference area for noise calculation. The proposed method follows Usamentiaga et al. [36], with the reference region defined as a concentric, enlarged area surrounding the defect ROI. This dynamic adaptation of the reference region to the local thermal context of each defect improves the robustness of the calculated SNR values. In this study, no post-processing techniques are applied to the thermographic data as the main objective is to assess the reliability of the raw signal in relation to surface roughness resulting from the build orientation. Although the potential of advanced post-processing methods—such as statistical filtering and signal reconstruction—is recognized in the literature to improve the detectability of defects [37, 38], these are excluded in this first step.

Following defect detection, a measurement procedure was developed to automatically determine the size

of defects in thermographic images. Methods examined included: i) fitting a Gaussian curve to the temperature profile intersecting the defect and assessing the peak width or the width at half maximum; ii) mathematical analysis of the temperature profile across the defect or its spatial derivative. As for the SNR calculation, the measurement procedure was repeated 6 times for each experiment.

3 Results and discussion

The experimental procedure followed a sequential approach: X-ray computed tomography was first performed, followed by surface analysis using confocal microscopy. The samples were then painted, and thermographic inspections were subsequently carried out.

3.1 Tomography

The tomographic analysis confirmed the successful fabrication of all artificially embedded defects in the samples. Scans revealed many defects were partially filled with sintered powder due to inaccessibility or strong sintering of the powder [39]. This allowed us to assess how the presence of sintered powder influences Joule heating and thermographic detection, particularly whether it behaves like solid material or a void in active thermography. This is crucial for future applications to closed defects, where sintered powder is unavoidable. Results showed that sintered powder did not significantly hinder defect detection and behaved thermally like a hollow region. For example, a defect with a nominal diameter of 1 mm and a nominal depth of 0.5 mm was successfully detected from the side target surface. The effective depth was 1.01 mm considering only fully consolidated material, while including powder would result in 8.92 mm, well beyond the detection range of the technique and clearly contrary to the correct experimental detection. This led us to evaluate only the thickness of the dense material for depth measurement, ignoring the presence of powder, as illustrated in Fig. 4. This preliminary result indicates that the powder's thermal and electrical conductivities are relatively low, consistent with literature data [23].

CT scans were used to determine the actual size and depth of defects, leading to the results in Table 2. The size (diameter) measurements generally showed good accuracy, with a maximum deviation from nominal values of + 28% for the Down sample. Depth measurements revealed more marked deviations (Fig. 5). Both H-Up and H-Down specimens show a greater depth of all defects. This result correlates with a larger overall width of the two samples: 10.47 mm for H-Up and 10.55 mm for H-Down. These deviations are due to typical manufacturing tolerances, but also to the excess of consolidated material onto downskin surfaces, which increases defect depth, with the deviation being comparatively higher for shallower defects, as seen with a + 136% in the H-Down sample. In the H-Up sample, the downskin effect occurs within the hole closure, where the first layer closing the hole melts additional material, reducing the hole length and consequently increasing its depth. The H-Down-Plat sample, produced with the same orientation under different conditions, deviated from this trend and showed a width reduction of -9.5%, resulting in a significant reduction in effective defect depth. The H-Side sample showed a moderate deviation with a width of 9.95 mm, slightly below nominal, reducing defect depth.

Table 2 also reports the values for circularity, varying with build orientation. Most defects were aligned along the Z-axis and had a generally high circularity (average 0.73). A notable exception is the H-Side specimen whose defects, aligned along the Y-axis, are exposed to downskin

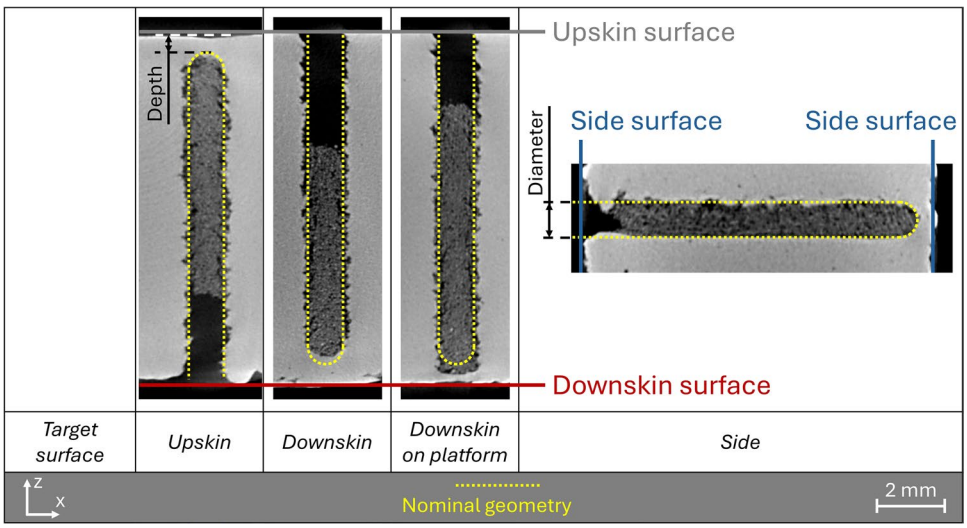

Fig. 4 Tomographic images of the section of defect S1D0.5 in the four samples, oriented according to the building direction

Table 2 Detailed results of the CT analysis for all the defects, classified in terms of target surface

Spec. ID	Nominal		Tomography								
	Size [mm]	Depth [mm]	Size [mm]			Depth [mm]			Size/depth	Circularity	
			Avg	S.D	Δ%	Avg	S.D	Δ%		Avg	S.D
H-Up	0.50	1.00	0.63	0.04	26	1.17	0.02	17	0.54	0.776	0.056
	0.50	0.25	0.62	0.04	24	0.44	0.06	76	1.41	0.781	0.052
	1.00	2.00	1.15	0.05	15	2.20	0.08	10	0.52	0.751	0.054
	1.00	0.50	1.15	0.05	15	0.68	0.1	36	1.69	0.757	0.046
H-Side	0.50	1.00	0.49	0.02	−2	0.90	0.03	−10	0.54	0.555	0.129
	0.50	0.25	0.49	0.02	−2	0.50	0.03	100	0.98	0.506	0.124
	1.00	2.00	1.02	0.02	2	1.80	0.01	−10	0.57	0.672	0.055
	1.00	0.50	1.01	0.02	1	0.54	0.01	8	1.87	0.632	0.063
H-Down	0.50	1.00	0.64	0.02	28	1.28	0.03	28	0.50	0.800	0.048
	0.50	0.25	0.64	0.02	28	0.59	0.03	136	1.08	0.774	0.055
	1.00	2.00	1.16	0.02	16	2.35	0.04	18	0.49	0.631	0.086
	1.00	0.50	1.16	0.02	16	0.89	0.01	78	1.30	0.631	0.085
H-Down-plat	0.50	1.00	0.58	0.04	16	0.54	0.04	−46	1.07	0.692	0.099
	0.50	0.25	0.58	0.05	16	0.20	0.03	−20	2.90	0.681	0.079
	1.00	2.00	1.11	0.03	11	1.42	0.04	−29	0.78	0.693	0.061
	1.00	0.50	1.11	0.03	11	0.18	0.03	−64	6.17	0.689	0.065

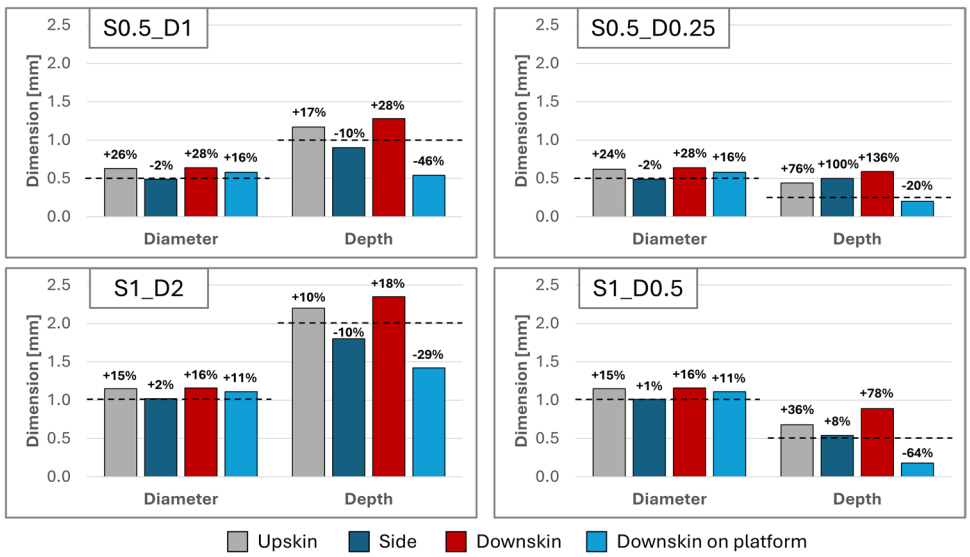

Fig. 5 Diameter and depth measured by tomography for defects under different target surface types. The dashed line represents the nominal value

Table 3 Roughness parameters of the target surfaces: Sa = arithmetical mean height, Sq = root mean square height, Sz = maximum height, Sp = maximum peak height, Sv = maximum valley depth, Ssk = skewness, Sku = kurtosis

Surface	Sa [μm]	Sq [μm]	Sz [μm]	Sp [μm]	Sv [μm]	Ssk	Sku
Upskin	7.0	8.7	61.0	32.7	28.3	−0.1	3
Side	38.4	45.9	278.2	142.5	135.8	0	2.3
Downskin	20.0	25.5	191.2	75.7	115.5	−0.5	3.5
Downskin on platform	12.3	16.3	149.9	55.3	94.5	−0.7	5.1

building conditions leading to reduced circularity (average 0.59). The table also shows the actual value of the ratio between size and depth, to be used as a reference for mapping the detection capability.

3.2 Surface analysis

The build orientation not only affects significantly the formation and geometry of seeded defects, but also the morphology of the target surfaces. Confocal surface measurements are summarized in Table 3, with the corresponding 3D topography maps in Fig. 6.

The upskin surface exhibited the smoothest topology with the lowest average areal roughness. The result is well-known in literature: the molten material solidifies in contact with gas, unaffected by satellites or surrounding powder particles [19]. The side surface displayed the highest roughness values, reflecting pronounced surface irregularities caused by the adhesion of satellite particles and the superimposition of the layers. Such features are expected to have a negative impact on thermographic inspection. Although the downskin and downskin-on-platform surfaces share the same build orientation, their morphology differs due to distinct build conditions: downskin-on-platform is in direct contact with the build plate, while downskin faces loose powder particles. Both surfaces showed intermediate average roughness values with negative skewness indicating a profile dominated by valleys rather than peaks.

3.3 IR thermography setup

3.3.1 Time evolution

When defining a reliable methodology for defect inspection, the first crucial step is selecting the most suitable frame for analysis. Figure 7 shows a sequence of the first five frames acquired after applying the electrical current, as well as two additional frames to show the long-term evolution. The SNR of the defect S1_D0.5 is indicated on each frame. The defect is most visible in the early frames, when the highest SNR is measured. Over time, thermal conduction smooths out temperature gradients, making defects less distinguishable. As a result of this analysis, the frame with the highest SNR, usually the second or third after excitation, was selected for the test protocol. Based on these results, the excitation time was reduced to 5 s. Further recommendations from this preliminary study are as follows.

– A relatively low-cost infrared camera, like the one used, is adequate for the intended application. However, a higher frame-rate camera could potentially improve sensitivity by capturing more frames with even higher SNR. In this study, the low frame-rate system provided only 2–3 usable frames with high SNR. A faster acquisition rate would likely allow the capture of additional high-quality frames that occur within the initial moments of thermal excitation but are missed due to the limited temporal resolution of the current setup.

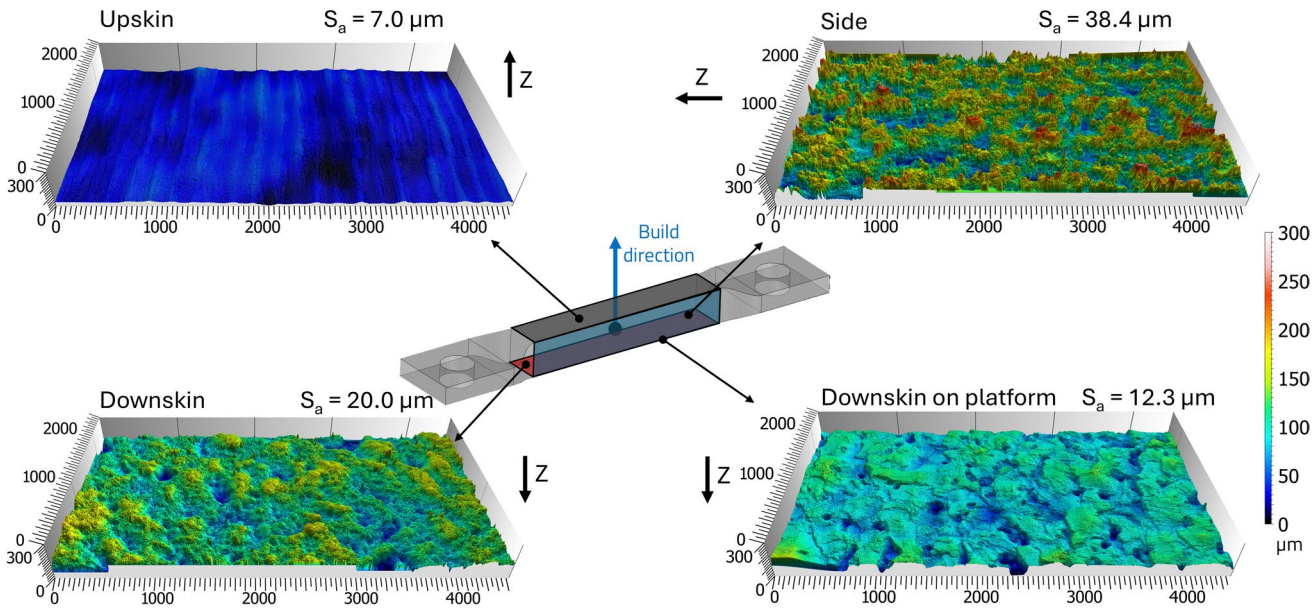

Fig. 6 Topology maps of the different target surfaces

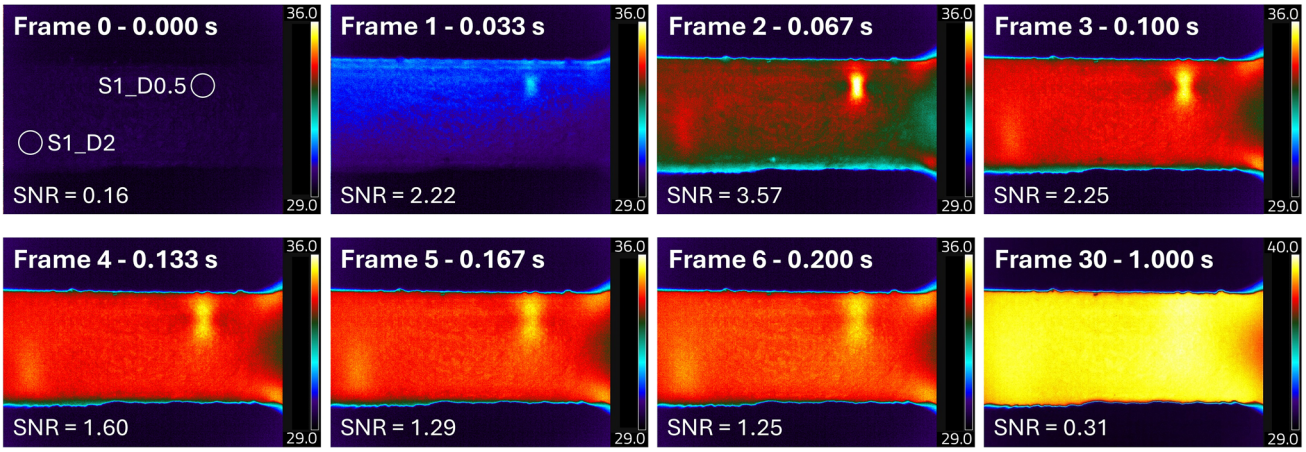

Fig. 7 Thermal images of the H-down_platform sample at different times after the current was applied (frame 0). The defect at the bottom left is S1_D2, the one at the topright is S1_D0.5. The SNR values refer to S1_D0.5

– Detection time is less than a few tenths of a second, making the technique suitable for rapid quality control in mass production environments.

3.3.2 Measurement procedure

After selecting the optimal frame capturing the defect, the next step is developing a robust, replicable procedure for the quantitative measurement of defect size based on thermographic data analysis. As shown in Fig. 8, this process involves four main steps. First, an additional rectangular ROI (Measurement ROI) is defined, including the defect and surrounding material along the i-axis. The rectangle should have a large base crossing the defect in the direction of current flow (i) and a height smaller than the hot area in the j-direction. This ensures that the full thermal response is evaluated and a complete dataset is obtained. Next, a temperature profile is extracted by averaging temperature values along the j-axis for each i-coordinate (Fig. 8b) and fitting the result with a three-term Gaussian function (Fig. 8c). After comparing several alternatives, this fitting function was chosen for its effective modeling of the experimental temperature profile data. The first derivative of the fitted Gaussian curve is then calculated. Defect size is determined as the

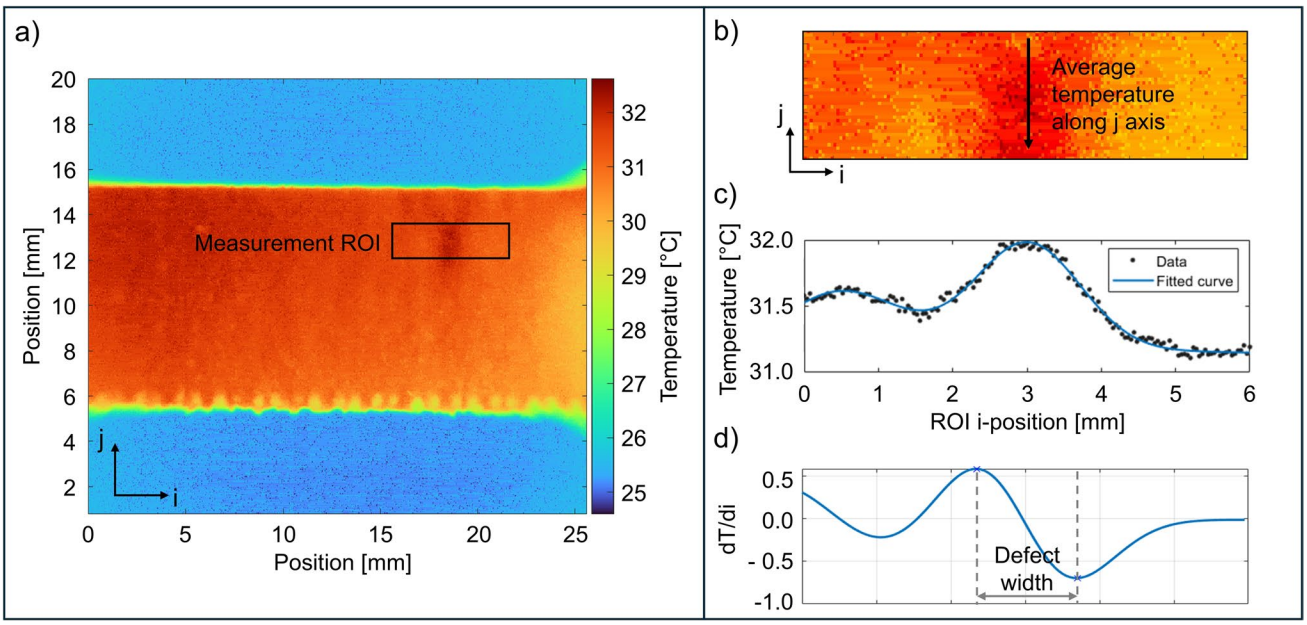

Fig. 8 Data processing procedure for defect size measurement: **a** positioning of the measurement ROI, **b** magnification of the selected ROI, **c** temperature profile along the ROI in the i-direction, **d** spatial derivative of the temperature profile

i-distance between the local maximum and minimum points of the derivative (Fig. 8d). This method proved robust and stable, minimizing the influence of arbitrary ROI definition and benefiting from unambiguous identification of derivative curve points.

The defined procedure for placing the measurement ROI is currently carried out manually. However, it could be automated using an algorithm that, after identifying the area of the sample to be analysed, scans the entire surface by calculating the SNR over a predefined grid. An alternative approach would be to automatically detect defects using trained computer vision algorithms.

3.3.3 Effect of the excitation current

To assess the sensitivity of the methodology to variations in excitation conditions, an analysis was performed by varying the electric current during thermographic tests. The resulting SNR and defect diameter were measured over a current range from 20 to 800 A (Fig. 9). Current variation had no significant effect on defect contrast or size: both parameters remained essentially stable over the tested range. This demonstrates the robustness of the inspection procedure against electrical current fluctuations. This result also confirms that low-current power supplies can be used without compromising detection accuracy, making the method cost-effective and energy-efficient for quality control.

The overall inspection protocol is summarized in the flowchart in Fig. 10.

3.4 IRT detectability as a function of the surface morphology

The study results on defect detectability based on size, depth, and target surface are summarized in Fig. 11, with SNR averaged over 6 test repetitions as the KPI. The four diagrams correspond to the samples analyzed: defects are plotted by actual size and depth measured by CT scans and categorized according to their detectability using a colour code. Mean SNR values are displayed next to the coloured dots.

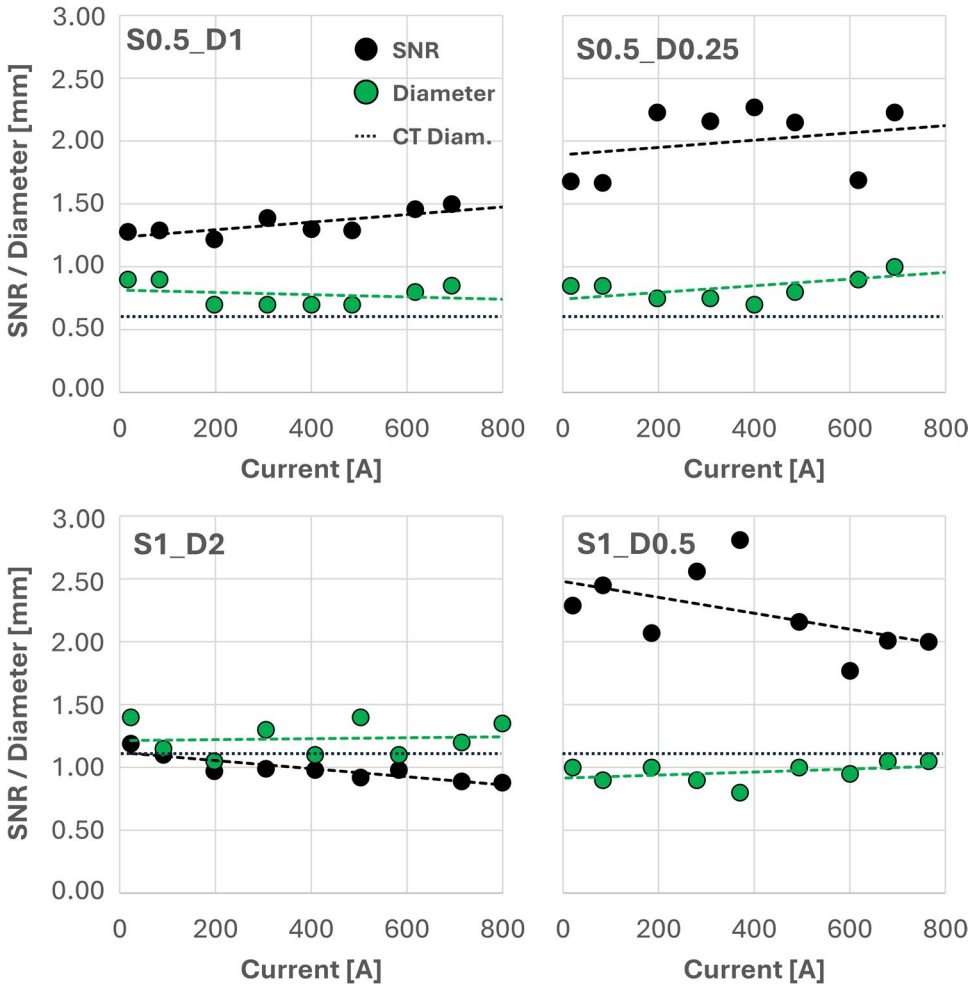

Fig. 9 Effect of the excitation current on the SNR and defect size for the four defects of the sample H-down_plat

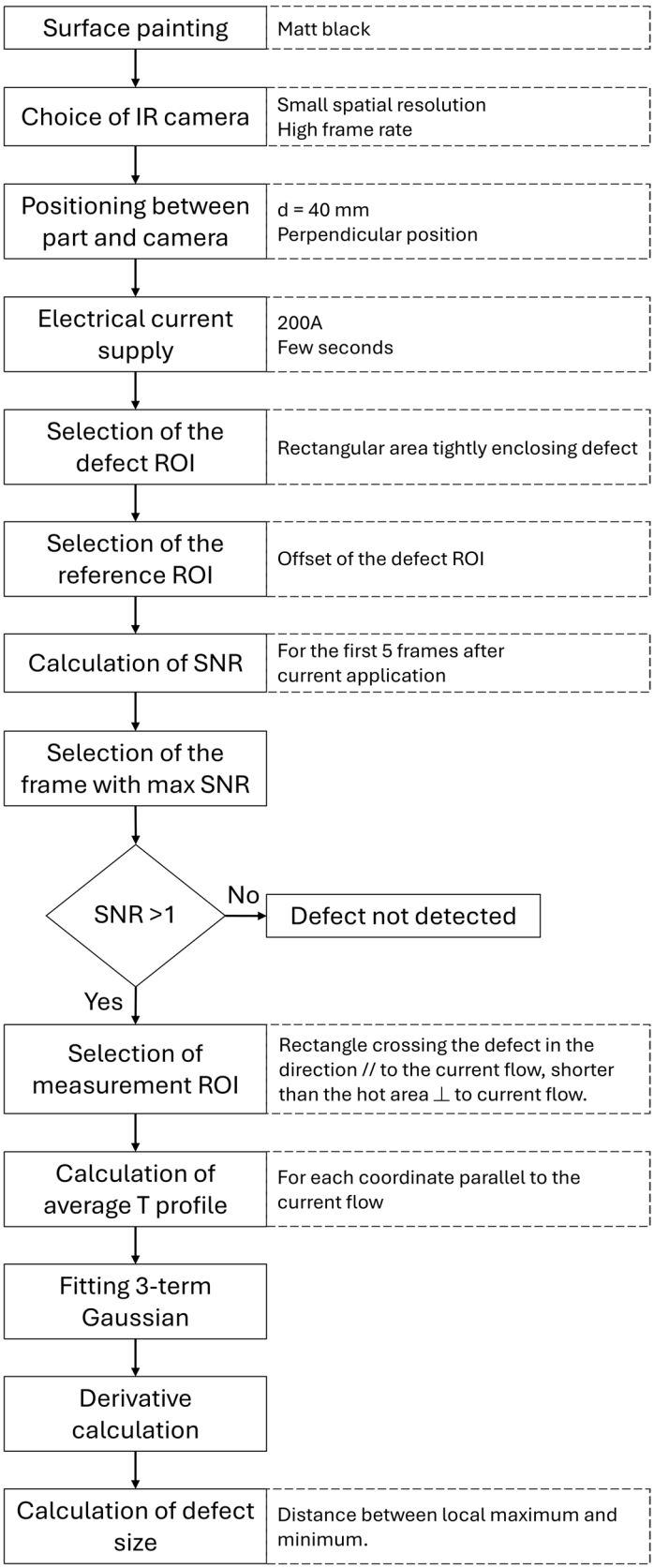

Fig. 10 Flowchart of the inspection protocol developed for IR thermography analysis

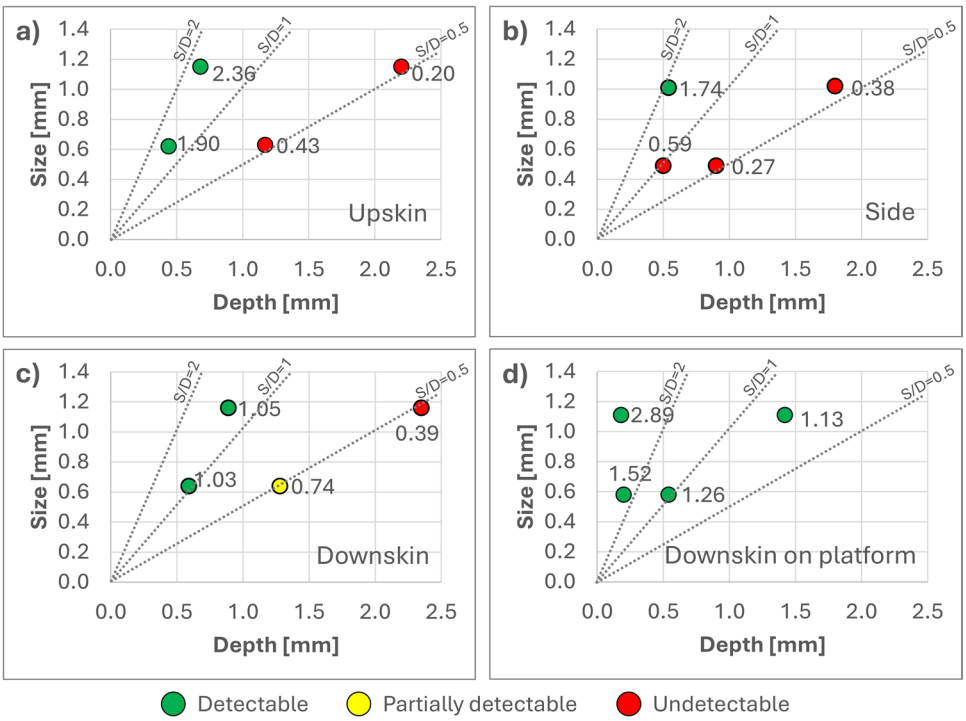

Fig. 11 Detectability of defects in terms of SNR as a function of their actual size, depth and target surface: **a** upskin, **b** side, **c** downskin and **d** downskin on platform

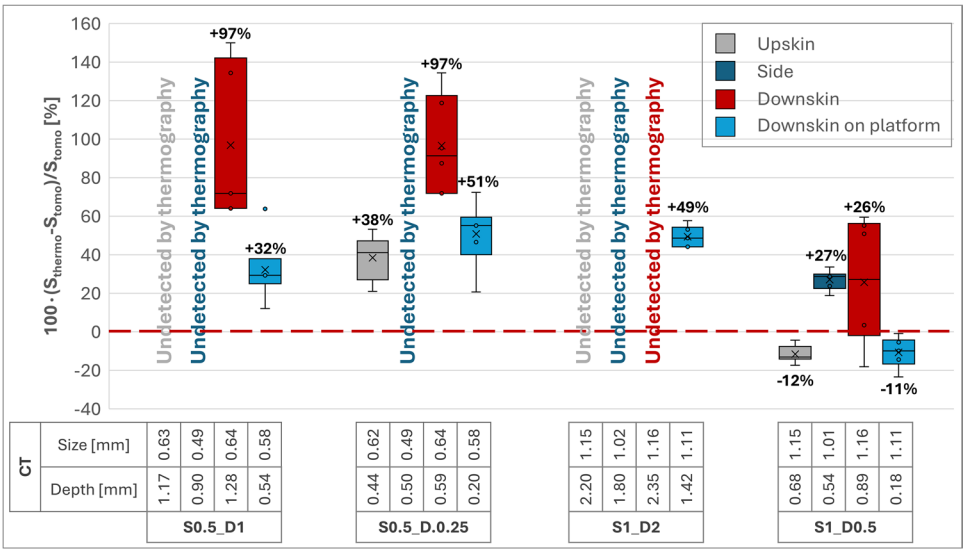

Fig. 12 Percentage deviation between the defect diameter measured with thermography and tomography, plotted for the different defect sizes and depths with a classification by target surface. The tomography results are also shown, to easily relate actual and nominal dimensions of defects

Looking at the effect of actual size and depth on detectability, a clear trend shows that the largest and shallowest defect (S1_D0.5) is consistently detected with SNR greater than 1 across all surfaces, though detectability decreases from the smoothest to the roughest surfaces.

Detectability decreases with decreasing size and increasing depth. Although the defects were nominally the same for the four target surfaces, the actual size and depth varied due to manufacturing accuracy, resulting in a different position of the experimental points covering a lower depth range for the downskin on platform, for example, which in combination with the relatively smooth surface led to the detection of all defects.

The analysis confirmed that defect depth is critical for detectability: defects deeper than 1.5 mm remained undetected regardless of their size, indicating a practical detection limit within this range. Surface roughness also plays a decisive role; defects under rough side surfaces were undetected even at shallower depths. In the downskin sample, high roughness and deeper than nominal defect locations contributed to poor detectability. Conversely, in the case of the smoothest surface (downskin on platform), it was possible to detect a defect with a diameter of

1.11 mm at a depth of 1.42 mm—thus overcoming the conventional size-to-depth ratio limit of 1. This result highlights the potential of Joule excitation, whose generative nature induces a more localized and pronounced thermal response at defect sites, enhancing the signal-to-noise ratio even for small or deep defects that would typically remain undetected using conventional surface-based excitation methods.

For all surfaces, easy detection occurs in the upper-left plot area, with SNR decreasing towards the lower-right, indicating a boundary curve shifting with surface roughness.

3.5 IRT dimensional measurements

The accuracy of defect size measurement by thermographic testing can be evaluated in Fig. 12, using CT results as reference data. The percentage deviation between the diameters measured by thermography (as per the method in Fig. 8) and CT is plotted against defect size and depth, classified by target surface. Dimensions were evaluated only for defects with SNR above the detectability threshold to assess the overall significance of the proposed method in spotting and sizing defects. The largest and shallowest defect (S1_D0.5), which exhibited the highest detectability with the neatest thermographic signals, also achieved the highest measurement accuracy. For other defects, rougher surfaces resulted in lower SNR and, even when detection was successful, a significant reduction in measurement accuracy. This finding is particularly evident for downskin surfaces, showing the highest percentage deviations between IRT and CT measurements. Of the two main factors influencing detectability—surface morphology and defect depth—the former is decisive for measurement accuracy. For the H-down sample, the measurement accuracy for a defect at 0.59 mm depth is comparable to that at 1.28 mm, suggesting that depth alone does not determine accuracy. The same applies to the H-down_plat sample, showing no clear correlation between defect depth and measurement deviation.

4 Conclusions

This study contributed to the application of active IRT with Joule excitation as a cost-effective and rapid non-destructive inspection technique for detecting sub-surface defects in PBF-EB components. Specifically, the research: i) proposed a robust and replicable methodology; ii) quantified the detection capability of the method, on a simplified set of defects, but focusing on surface morphology; iii) compared detection capability and measurement accuracy with more time- and cost-intensive tomography.

The experimental framework not only highlights the potential of active thermography for industrial quality control, but also critically assesses factors affecting detectability, particularly morphology of the target surface. This foundation supports the development of detectability maps and refined inspection protocols, positioning IRT as a viable alternative to tomography depending on location and size of potentially critical defects for a given component. Open cylindrical defects were incorporated into samples to develop the procedure and relate the results to the typical PBF-EB surface finishes.

Key concluding remarks are:

- Sintered powder partially filling the defects had no significant effect on thermographic detection and was therefore treated as voids.
- A robust inspection procedure was established by collecting the best practices and defining KPIs for detectability. Sensitivity analysis showed negligible influence of excitation current on defect visibility and dimensions. A Gaussian-based automatic procedure for defect size measurement was implemented.
- Defect size and depth as well as surface morphology significantly influence detection. Defects shallower than ~ 1.5–2.0 mm and larger in size were consistently detected with SNR values above 1, while deeper or smaller defects, particularly under rough surfaces such as the side surface, often remained undetected.
- Surface roughness severely limits detection performance and thermographic dimensional measurements, sometimes outweighing the influence of depth. Comparison with CT data confirmed higher measurement deviations for defects beneath rough surfaces, emphasizing the critical role of surface finish in thermographic inspections.

Future work will focus on automating the defect detection workflow by developing trained algorithms capable of identifying defects directly from thermal data. In parallel, the test protocol will be extended to closed defects—i.e., defects where powder removal is not possible—to confirm that their thermal signatures do not differ from those of open defects. These developments will strengthen both the robustness and applicability of the protocol proposed in this study.

5 Conflict of interest

The authors declare no competing interests.

Author contributions Conceptualization: M.G., L.D., and G.R. Funding acquisition: M.G., L.D. Resources: L.D. Investigation: S.DG. and G.C. Formal analysis: S.D. and G.C. Software: S.D. and G.C. Visualization: S.DG. and S.D. Supervision: M.G. and G.R. Writing: All authors.

Funding Open access funding provided by Università degli Studi di Modena e Reggio Emilia within the CRUI-CARE Agreement. The authors received financial support under the National Recovery and Resilience Plan (NRRP), Mission 4, Component 2, Investment 1.1, Call for tender No. 104 published on 2.2.2022 by the Italian Ministry of University and Research (MUR), funded by the European Union – NextGenerationEU– Project Title: Innovative additively manufactured parts inspection via non-destructive methods based on thermography and Computed Tomography (INTACT) – CUP E53D23003820006 - Grant Assignment Decree No.1385, 01/09/2023 adopted by the Italian Ministry of Ministry of University and Research (MUR).

Data availability Data available on request.

References

1. Deane S, Avdelidis NP, Ibarra-Castanedo C et al (2019) Application of NDT thermographic imaging of aerospace structures. Infrared Phys Technol 97:456–466. https://doi.org/10.1016/j.infrared.2019.02.002
2. Galati M, De Giorgi S, Rizza G et al (2025) A review of ex-situ, in situ and artificial intelligence-based thermographic measurements in additively manufactured parts. J Nondestr Eval 44:68. https://doi.org/10.1007/s10921-025-01195-9
3. Ibarra-Castanedo C, Tarpani JR, Maldague XPV (2013) Nondestructive testing with thermography. Eur J Phys 34:S91–S109. https://doi.org/10.1088/0143-0807/34/6/S91
4. Usamentiaga R, Venegas P, Guerediaga J et al (2014) Infrared thermography for temperature measurement and non-destructive testing. Sensors 14:12305–12348. https://doi.org/10.3390/s140712305
5. Bagavathiappan S, Lahiri BB, Saravanan T et al (2013) Infrared thermography for condition monitoring – a review. Infrared Phys Technol 60:35–55. https://doi.org/10.1016/j.infrared.2013.03.006
6. Yang R, He Y (2016) Optically and non-optically excited thermography for composites: a review. Infrared Phys Technol 75:26–50. https://doi.org/10.1016/j.infrared.2015.12.026
7. Connolly MP (1991) A review of factors influencing defect detection in infrared thermography: applications to coated materials. J Nondestr Eval 10:89–96. https://doi.org/10.1007/BF00567440
8. D'Accardi E, De Finis R, Dell'Avvocato G et al (2024) Conduction thermography for non-destructive assessment of fatigue cracks in metallic materials. Infrared Phys Technol 140:105394. https://doi.org/10.1016/j.infrared.2024.105394
9. Lecompagnon J, Hirsch PD, Rupprecht C, Ziegler M (2023) Nondestructive thermographic detection of internal defects using pixel-pattern based laser excitation and photothermal super resolution reconstruction. Sci Rep 13:3416. https://doi.org/10.1038/s41598-023-30494-2
10. Moskovchenko A, Švantner M, Vavilov V, Chulkov A (2022) Analyzing probability of detection as a function of defect size and depth in pulsed IR thermography. NDT and E Int 130:102673. https://doi.org/10.1016/j.ndteint.2022.102673
11. He Y, Pan M, Luo F (2012) Defect characterisation based on heat diffusion using induction thermography testing. Rev Sci Instrum. https://doi.org/10.1063/1.4756211
12. Wieczorowski M, Rozanski L, Gapinski B, Krolczyk MG (2014) Investigations regarding the influence of surface topography on emissive properties of material. Appl Mech Mater 657:402–406. https://doi.org/10.4028/www.scientific.net/AMM.657.402
13. Wen C-D, Mudawar I (2006) Modeling the effects of surface roughness on the emissivity of aluminum alloys. Int J Heat Mass Transf 49:4279–4289. https://doi.org/10.1016/j.ijheatmasstransfer.2006.04.037
14. Yu K, Liu Y, Liu D, Liu Y (2019) Normal spectral emissivity characteristics of roughened cobalt and improved emissivity model based on Agababov roughness function. Appl Therm Eng 159:113957. https://doi.org/10.1016/j.applthermaleng.2019.113957
15. Avdelidis NP, Delegou ET, Almond DP, Moropoulou A (2004) Surface roughness evaluation of marble by 3D laser profilometry and pulsed thermography. NDT E Int 37:571–575. https://doi.org/10.1016/j.ndteint.2004.03.002
16. Sauer C, Höfflin D, Schiffler A, Hartmann J (2024) Active thermography in PBF-LB/M with the synchronized path infrared thermography. Procedia CIRP 124:283–286. https://doi.org/10.1016/j.procir.2024.08.118
17. Pakkanen J, Calignano F, Trevisan F et al (2016) Study of internal channel surface roughnesses manufactured by selective laser melting in aluminum and titanium alloys. Metall Mater Trans A Phys Metall Mater Sci 47:3837–3844. https://doi.org/10.1007/s11661-016-3478-7
18. Kim GD, Oh YT (2008) A benchmark study on rapid prototyping processes and machines: quantitative comparisons of mechanical properties, accuracy, roughness, speed, and material cost. Proc Inst Mech Eng Part B J Eng Manuf. https://doi.org/10.1243/09544054JEM724
19. Galati M, Rizza G, Defanti S, Denti L (2021) Surface roughness prediction model for electron beam melting (EBM) processing Ti6Al4V. Precis Eng 69:19–28. https://doi.org/10.1016/j.precisioneng.2021.01.002
20. Oster S, Breese PP, Ulbricht A et al (2024) A deep learning framework for defect prediction based on thermographic in-situ monitoring in laser powder bed fusion. J Intell Manuf 35:1687–1706. https://doi.org/10.1007/s10845-023-02117-0
21. Ulbricht A, Mohr G, Altenburg SJ et al (2021) Can potential defects in LPBF be healed from the laser exposure of subsequent layers?. A quantitative study. Metals (Basel) 11:1012. https://doi.org/10.3390/met11071012
22. Körner C (2016) Additive manufacturing of metallic components by selective electron beam melting—a review. Int Mater Rev, pp 1–17
23. Rizza G, Galati M (2024) Powder bed fusion with electron beam: the interplay of sintering, porosity, and coordination number in modelling the powder thermal conductivity through a novel tortuosity formulation. Int J Heat Mass Transf 234:126055. https://doi.org/10.1016/j.ijheatmasstransfer.2024.126055
24. Vayssette B, Saintier N, Brugger C et al (2019) Numerical modelling of surface roughness effect on the fatigue behavior of

Ti-6Al-4V obtained by additive manufacturing. Int J Fatigue. https://doi.org/10.1016/j.ijfatigue.2019.02.014
25. Denti L, Sola A (2019) On the effectiveness of different surface finishing techniques on A357.0 parts produced by laser-based powder bed fusion: surface roughness and fatigue strength. Metals 9:1284. https://doi.org/10.3390/met9121284
26. ASTM International (2023) ISO/ASTMTR52905 - additive manufacturing of metals - nondestructive testing and evaluation - defect detection in parts. ASTM International100 Barr Harbor Drive, PO Box C700, West Conshohocken, PA 19428–2959
27. Galati M, Defanti S (2024) Additive manufacturing of locally weakened parts to obtain a designed fracture. Metals Mater Int. https://doi.org/10.1007/s12540-023-01506-7
28. D'Accardi E, Altenburg S, Maierhofer C et al (2019) Detection of typical metal additive manufacturing defects by the application of thermographic techniques. In: The 15th international workshop on advanced infrared technology and applications. MDPI, Basel Switzerland, p 24
29. Kolb CG, Zier K, Grager J-C et al (2021) An investigation on the suitability of modern nondestructive testing methods for the inspection of specimens manufactured by laser powder bed fusion. SN Appl Sci 3:713. https://doi.org/10.1007/s42452-021-04685-3
30. Shi W, Ren Z, He W et al (2021) A technique combining laser spot thermography and neural network for surface crack detection in laser engineered net shaping. Opt Lasers Eng 138:106431. https://doi.org/10.1016/j.optlaseng.2020.106431
31. D'Accardi E, Ulbricht A, Krankenhagen R et al (2021) Capability of active thermography to detect and localize pores in metal additive manufacturing materials. IOP Conf Ser Mater Sci Eng 1038:012018. https://doi.org/10.1088/1757-899X/1038/1/012018
32. D'Accardi E, Krankenhagen R, Ulbricht A et al (2022) Capability to detect and localize typical defects of laser powder bed fusion (L-PBF) process: an experimental investigation with different non-destructive techniques. Prog Addit Manuf 7:1239–1256. https://doi.org/10.1007/s40964-022-00297-4
33. Höfflin D, Sauer C, Schiffler A et al (2024) Active thermography for in-situ defect detection in laser powder bed fusion of metal. J Manuf Process 131:1758–1769. https://doi.org/10.1016/j.jmapro.2024.09.085
34. Höfflin D, Sauer C, Schiffler A, Hartmann J (2022) Process monitoring using synchronized path infrared thermography in PBF-LB/M. Sensors 22:5943. https://doi.org/10.3390/s22165943
35. Madruga FJ, Ibarra-Castanedo C, Conde OM et al (2010) Infrared thermography processing based on higher-order statistics. NDT E Int 43:661–666. https://doi.org/10.1016/j.ndteint.2010.07.002
36. Usamentiaga R, Ibarra-Castanedo C, Maldague X (2018) More than fifty shades of grey: quantitative characterization of defects and interpretation using SNR and CNR. J Nondestr Eval 37:25. https://doi.org/10.1007/s10921-018-0479-z
37. D'Accardi E, Palumbo D, Galietti U (2022) Experimental procedure to assess depth and size of defects with pulsed thermography. J Nondestr Eval 41:41. https://doi.org/10.1007/s10921-022-00870-5
38. Wang F, Jiang Z, Liu Y et al (2025) Enhancing defect detection in active infrared thermography using adaptive background suppression techniques. J Therm Anal Calorim 150:8163–8176. https://doi.org/10.1007/s10973-024-13668-6
39. Rizza G, Galati M, Antonioni P, Iuliano L (2023) Effect of the sintering conditions on the neck growth during the powder bed fusion with electron beam (PBF-EB) process. J Manuf Mater Process 7:55. https://doi.org/10.3390/jmmp7020055